Synthesis, characterization and thermal stability of SnAg and SnAgCu nanoparticles

S. Delsante[a,b,*], R. Novakovic[b], G. Borzone[a,b]

[a]Department of Chemistry and Industrial Chemistry, Genoa University and Genoa Research Unit of INSTM, Via Dodecaneso 31, I-16146, Genoa, Italy

[b]Institute of Condensed Matter Chemistry and Energy Technologies, National Research Council (ICMATE-CNR), Via de Marini 6, I-16149 Genoa, Italy

* Corresponding author: simona.delsante@unige.it

Abstract

The melting temperature and melting enthalpy of SnAg and SnAgCu (SAC) nanocrystals with diameters of approximately 30 nm was determined and, by means of Differential Scanning Calorimetry (DSC) a depression melting temperature of 7-10°C was observed for both systems. The new experimental results were compared to the predicted values as well as available datasets. X-ray diffraction (XRD) analysis was performed to characterize the as-prepared and heat treated samples. Scanning electron microscopy (SEM and FE-SEM) analysis was carried out to study the morphology, microstructure and phase evolution of the as-synthesized particles before and after the heating process.

***Keywords**: A. SnAg; A. SnAgCu; A. nanoparticles; C. melting point depression; C. melting enthalpy; D. calorimetry*

1. Introduction

Thanks to the excellent metallurgical characteristics of Pb-Sn alloys, these solders have been found to offer good all-round properties for wettability, thermal cycling, shiny joints and low costs. However, starting from July 2006, for environmental and health reasons, a resolution to ban the use of solders containing Pb in all new electronic devices has been adopted [1-4]. As a result, there has been considerable interest in the field of low temperature interconnect technologies and materials, mainly based on Sn often containing Ag, Bi, Cu and Zn as the major alloying elements and some minor additions. A new series of alloys such as SnAgCu (SAC), were developed and are currently in use [5-9].

However, all these alternative solders do not completely meet the industrial requirements (i.e. comparable Pb-Sn melting temperature, equally good wetting, strong and reliable connections, etc.) [10], and the development of nano-solder alloys and their manufacturing in the form of Pb-free pastes [11,12] has been considered and extensively investigated. Furthermore, a recent study by Luc et al. [13] highlights the potential application of SnAg bimetallic electrocatalyst nanoparticles for catalytic CO_2 conversion, having an ultrathin partially oxidized SnO_x shell and a core of Ag_3Sn which is responsible for high electronic conductivity.

As a matter of fact, the potential applications of nanoalloys in different fields generated the need to obtain reliable thermodynamic data necessary to determine the stability of the nanoalloy systems, develop materials property databases, as well as carry out theoretical calculations to substantiate experimental work [14-17].

There are attempts to extend the thermodynamic framework used in the study of bulk alloys to nanoscale systems, of at least a few nanometers. The most complete thermodynamic equilibrium description of a nanoalloy was achieved by determining its phase diagram, as a function of size, composition and temperature [19-21]. Indeed, the melting temperature depression due to nano size effect has been well established both experimentally and theoretically. In 1909 Pawlow developed a thermodynamic model stating that the melting temperature of nanoparticles depends on the particle size [22]. The thermodynamics of solid-liquid phase equilibria in small particle systems has been initially studied by analysing the melting phenomena of pure metals and alloys [23-24]. Subsequently, other researchers [25-27] have investigated the variation of melting temperature with particle size and many theoretical models have been successfully applied. In particular, concerning the melting point depression of pure metals, the models taking into account different configurations of the solid metals, including grains embedded within a matrix, have been

developed [28]. Among the models reported in [26], those describing the reduction of the melting temperature in terms of macroscopic measurable thermodynamic and thermophysical quantities [23] together with an extended CALPHAD method used to assess the phase diagrams of nano-sized alloy systems [19,29,30], are appropriate for binary and ternary nanoalloys. Indeed, the nano-sized phase diagram will be shifted toward lower temperatures in comparison to its bulk counterpart due to size effects in the nanoscale regime, indicating the melting temperature depression in all the alloys under investigation [18,27,31].

The present study examines the thermal behaviour of SnAg and SAC (SnAgCu) nanoalloys near the eutectic composition. Experimental results are discussed and compared with values predicted using the homogeneous melting (HM) model as well as with the literature data.

2. Materials and experimental methods

2.1. Chemicals and synthesis

Various experimental techniques for nanoparticles (NPs) production are reported in literature. Both physical and chemical methods as well as a combination of both have been developed, showing that the processing method can significantly affect the characteristics of the produced nanoparticles. Currently, various preparation methods for SnAg and SAC nanoparticles exist [32-35].

In this work, SnAg and SAC nanopowders were synthesized by simultaneous chemical reduction of metal ions by energetic reducing agents, such as sodium borohydride ($NaBH_4$), using phenanthroline as surfactant. All chemicals, listed below, were of analytical grade and were used as received without further purification: Copper (II) sulfate pentahydrate ($CuSO_4 \cdot 5H_2O$) (Panreac, 99.993 mass%);Tin (II) 2-ethylhexanoate ($C_{16}H_{30}O_4Sn$) (Alfa Aesar, 95 mass%); Tin(II) chloride ($SnCl_2$) (Carlo Erba, RPE grade); Silver nitrate ($AgNO_3$) (Merck, 99.8 mass%); 1,10-phenanthroline ($C_{12}H_8N_2H_2O$) (Alfa Aesar, 99 mass%). Water MQ and anhydrous methanol (CH_3OH) (Sigma Aldrich, 98.8 mass%) were used as solvents.

The current synthetic procedure is based on the method developed by [36-38]. All syntheses were carried out under argon atmosphere in a five-neck round-bottom flask (1000 ml) equipped with a dropping funnel. The metal salt precursors were mixed in the selected solvent and maintained under vigorous stirring to obtain a homogeneous solution. The $NaBH_4$ solution was added dropwise to the flask thoroughly degassed with argon. Generally, the synthesis was carried out at

25°C, with the exception of sample SA_3 prepared at 0°C, maintaining the flask in an ice bath for 2h before adding $NaBH_4$. The resulting fine black precipitate was filtered under argon and washed with absolute ethanol, dried 8 hours under Ar, passivated by air and subsequently the powders were manipulated in air.

Table 1 summarizes the synthesised and thermally treated SnAg and SAC nanopowders, together with the experimental results obtained after characterization.

2.2. Characterization techniques

The structural and morphological characterization of the samples was carried out by means of X-ray powder diffraction (XRD) and two different types of Scanning Electron Microscopes (SEM). The XRD analysis was performed using a Philips X'Pert MPD machine (Philips, Almeno, The Netherlands) equipped with a copper target, excited to 40 kV and 30 mA, and a solid state detector. The crystallite size was evaluated using the Scherrer equation [39].

A scanning electron microscope ZEISS SUPRA 40 VP with a field emission gun (FE-SEM), equipped with a high sensitivity "InLens" secondary electrons detector and with an EDX microanalysis OXFORD "INCA Energy 450 × 3" was used. In addition, a Zeiss Evo 40 (Carl Zeiss SMT Ltd, Cambridge, England) equipped with a Pentafet Link Energy Dispersive X-ray Spectroscopy (EDXS) system managed by the INCA Energy software (Oxford Instruments, Analytical Ltd., Bucks, U.K) was employed. Samples for FE-SEM analysis were suspended in ethanol and exposed to ultrasonic vibrations to reduce the level of aggregation. A drop of the resulting mixture was finally laid on a Lacey Carbon copper grid.

The thermal behaviour of the samples was investigated by a heat flux Differential Scanning Calorimetry (DSC) using a DSC111 SETARAM apparatus designed as a Calvet calorimeter, previously calibrated by measuring the melting temperature of metallic In, Sn, Pb and Zn (99.999 mass % purity). The temperature was obtained with an accuracy of ±0.5 °C. Around 60 mg of nanopowders were generally inserted in sealed Ta crucibles; in several cases open Al_2O_3 crucibles or closed quartz tubes were employed. The SnAg nanopowders were subjected to a thermal cycle at a heating/cooling rate of 5 °/min, from 20 °C up to 300 °C and back, whereas for SAC nanopowders a thermal cycle from 20 °C to 360 °C was employed. Before cooling, the samples were maintained at the maximum temperature for 10 minutes.

2.3. Melting temperature depression: Theory

Among overall properties of nanosized systems temperature dependent properties are strongly influenced by nanoparticle size. In 1909 Pawlow [22] postulated that the melting point depression occurs due to the large influence of the surface energy on nanosized particle properties. The large surface/volume ratio in nanosized particle systems (unary, binary, etc.) has significant effects on their thermodynamic properties and phase relations [18,21]. During the years, various thermodynamic models describing the melting temperature of metal nanoparticles as a function of their size have been assessed and recently reviewed by Barybin and Shapovalov 26]. Their experimental validation was done on both metals [23,24] and alloys [29-31,38]. All models are mainly expressed in terms of thermodynamic (bulk latent heat of fusion, bulk melting temperature) and thermophysical properties (density or volume of solid and liquid bulk phases; interfacial tensions liquid/vapour, liquid/solid, solid/solid). These are sometimes combined with adjustable parameters whose values were determined from the experimental data. Concerning the thermodynamic models used to study the melting behaviour of metallic nanoparticles, the critical points, such as the choice of input data, the definition of adjustable coefficients, as well as the need to choose various parameters simultaneously, make it difficult to find a "unique" model as an appropriate description of the experimental data. In addition, none of the models listed in[26] take into account the effects of the substrate on melting, that surely play an important role and affect the results of measurements due to the presence of a grain boundary at the cluster-substrate interface. Another problem is the coalescence of nanoparticles during measurements and identification of an individual nanosized particle or cluster.

In the present work the melting temperature depression of SnAg and SAC nanoalloys was analysed using the homogeneous melting model (HM model) [23]:

$$\Delta T = T_m^{bulk} - T_m(r) = \frac{2 \cdot T_m^{bulk}}{H_m^{bulk} \cdot \rho_s \cdot r} \left[\sigma_s - \sigma_L \cdot \left(\frac{\rho_s}{\rho_L} \right)^{2/3} \right] \quad (1)$$

Where $\Delta T = T_m^{bulk} - T_m(r)$ is the melting temperature depression, r is the nanoparticle radius and T_m^{bulk} and H_m^{bulk} are the melting temperature and molar heat of fusion of the bulk alloy, respectively. σ_s, σ_L, ρ_s, ρ_L are the surface energy and density of the solid and liquid phases, respectively.

It has been shown that an extended CALPHAD (Calculation of Phase Diagrams) method that takes into account the effect of surface energy on the total Gibbs energy of a nanosized system is appropriate for the assessment of its phase diagram [18]. The optimized phase diagram clearly indicates the melting temperature depression of a nanoalloy system [18,27,31]. The experimental results on lead free nanosolders [6,40-42] fully substantiate the validity of the CALPHAD method for nanosized systems with the lowest particle size limit of 4-5 nm [29-31].

3. Results and Discussion

3.1. SnAg NPs

The SnAg NPs synthesis was performed both without surfactant (SA_7 and SA_10) and using 1,10-phenanthroline as surfactant (see Table 1). Tin (II) 2-ethylhexanoate was always used as Sn precursor with the exception of sample SA_11 for which $SnCl_2$ was employed. All samples were characterized by XRD analysis before and after DSC analysis.

As an example, the XRD patterns of the as-synthesized SA_8 and SA_11 alloy nanoparticles are shown in Figs. 1 and 2. In the same figures, the XRD patterns of the samples after DSC heating cycle are inserted for comparison. In the as-synthesized samples, in addition to the peaks indexed as a tetragonal cell of β-Sn (t*I*4-βSn), the Ag_3Sn (o*P*8-βCu_3Ti) phase was found, indicating the successful alloying of Sn and Ag after the reduction process. No extra-peaks were observed. The same results were obtained for all SnAg samples which testify the good reproducibility of the employed synthesis route. By using the Scherrer equation, an average crystallite size dimension of 30 nm has been evaluated.

The melting temperatures (onset points) obtained by DSC for the SnAg NPs samples are given in Table 1. It should be underlined that no significant differences were observed in the DSC heating and cooling curves for the samples prepared with or without phenatroline as surfactant, or using $SnCl_2$ as precursor. On heating, an endothermic peak was systematically registered, and an average temperature of 214°C was measured; nevertheless, a minimum value of 211°C was obtained for the samples SA_10 and SA_11. This effect corresponds to a melting temperature depression of about 7 – 10 °C in comparison with the temperature of 221°C reported for the eutectic reaction L→ β-Sn + Ag_3Sn of the bulk alloys [43]. As an example, the DSC heating and cooling curves of SA_8 and SA_11 samples are shown in Figs. 3 and 4. Depending on nanoparticle dimensions and synthetic methods, the literature data reports different values for the melting temperature depression of SnAg NPs. Pande et al. [33] found a melting point as low as 128°C for

SnAg nanopowders prepared from the commercially available precursor salts (Sn(II)acetate and Ag(I) acetate or nitrate) in silicone oil. Sopousek et al. [29] reported a 11.2°C melting depression for 40 nm SnAg nanoparticles, fairly in agreement with the present results.

The thermal behaviour of the SnAg and SAC nanoalloys was thoroughly discussed in [29,44]. It is well known that Sn-rich alloys are highly prone to oxidation, which significantly increases by decreasing particle size [45,46]. Indeed, TEM (Transmission Electron Microscopy) analysis performed on Sn and SnBi NPs [38], SnAg and SAC NPs [29,42,44] indicates the presence of SnOx amorphous layer covering the surface of NPs. The SnOx (x=1, 2) crystalline phase formation detected by XRD in the samples analysed after DSC (Table 1) confirms the oxidation phenomena in NPs containing Sn. In particular, the XRD patterns (Figs. 1-2) show SnO peaks (t*P*4-PbO) only for samples subjected to DSC. In a few samples (SA_3, SA_10) traces of SnO_2 were also found.

In the DSC heating curve, an evident exothermic peak detected after the melting effect was observed only for the SA_11 sample, as shown in Fig. 4a. For the other samples, a trend similar to that observed for sample SA_8 (Fig. 3a) was recorded. In agreement with the results reported by Roshanghias et al. [44], this effect can be ascribed to the crystallization of the amorphous SnOx layer surrounding the metallic NPs.

It can be underlined that, after DSC, the XRD analysis of sample SA_8 shows a lower amount of SnO (≈ 8%) than sample SA_11 (≈ 24%), in agreement with the size of the exothermic effect registered after melting, which is almost negligible for SA_8 in comparison with SA_11 (Figs. 3a-4a). Unlike what has been observed by different authors [29,44], no additional effects around 260°C were recorded on the DSC curves.

During cooling, for all SnAg samples a series of broadened fluctuating exothermic peaks starting from approximately 200 up to 120°C was systematically observed (Figs. 3b – 4b), among which a sharper peak around 140°C, possibly corresponding to solidification. We assume that these broad peaks occur during freezing owing to a low nucleation probability related to the presence of the oxide layer on the surface of SnAg powders. This layer probably acts as a nucleation barrier and prevents the nanocrystals from completely coalescing. Indeed, after DSC measurements, the NP samples turn to micro sized metallic powders together with small SnOx particles on their surface. At low magnification (Fig. 5a, Secondary electron (SE) signal), the image of sample SA_8 after DSC shows particles with different sizes: the small ones correspond to SnOx particles and the big ones to SnAg alloy spheres. At higher magnification (Fig.5b, Backscattered electron (BSE) signal), in the

bigger particles it is possible to recognize the characteristic SnAg eutectic morphology (β-Sn+Ag_3Sn).

In literature, in most of the cases, overlooking the complexity of the solidification curves, only the DSC heating curves have been reported and in very few studies the cooling curves have also been showed [29,40,42]. The small magnification of the graphs together with the scarce comments on them does not allow a deep comparison with the present results. However, the sharper peak identified in this work around 140°C in the DSC curves of the SnAg samples (Figs. 3b-4b), is fairly in agreement with the temperature solidification range of 150-110°C observed by Sopoušek et al. [29] and the value of 109.2°C for the solidification peak reported by Jiang et al. [42].

From the area under the DSC nanoparticle melting curves a quantitative evaluation of the melting enthalpy equal to 49±2 J/g was obtained, in comparison to the corresponding value of 60.2 J/g for the Ag-96.5Sn(mass%) bulk alloy [47].

3.2. SAC NPs

Experimental investigations and reassessments of the Sn-Ag-Cu phase diagram established slightly different compositions and melting temperatures for the eutectic invariant reaction L→ (β-Sn) + Ag_3Sn+ Cu_6Sn_5, i.e. the Sn-3.24Ag-0.57Cu (mass.%) at 217.7 °C [48] and Sn-3.5Ag-0.9Cu (mass.%) at 217.2 °C [2,49,50].

In the present study four SAC samples with near eutectic composition have been prepared, as described in 2.1, using for all samples $SnCl_2$ as Sn precursor and phenanthroline as surfactant. The synthesis of SAC_1 and SAC_2 has been performed in anhydrous methanol, whereas SAC_3 and SAC_4 have been prepared in deaerated MQ water. Besides, following the indications by Yung et al. [41], one portion of the as-prepared SAC_4 sample was treated with citric acid for 1h (sample termed as SAC_5) and another one for 18h (sample termed as SAC_6), with the aim to remove SnO_x supposed to be formed on the NPs surface (Table 1).

The XRD patterns of all as-prepared SAC samples are very similar showing the diffraction peaks of Ag_3Sn, β-Sn and Cu_6Sn_5 (hP4-NiAs); no tin oxide was identified. The peaks of Ag_3Sn and β-Sn were easily recognizable, whereas the small amount of Cu_6Sn_5 was more detectable in the sample pattern after DSC. Likewise the SnAg samples, after heat treatment the presence of the SnO phase was detected; for the SAC samples synthesized in MQ water, traces of SnO_2 were also present. In figure 6 is inserted the XRD patterns of the as-synthesized sample SAC_2 together with the XRD patterns of this sample after DSC heating cycle.

The DSC analysis was performed with a scanning rate of 5°C/min in 20-300°C (SAC_1 and SAC_2 first cycle) or 20-360°C (SAC_2 second cycle, and the rest of the samples) temperature range.

The DSC curve obtained for SAC_1 evidenced that the sample was not exactly on the eutectic composition since, on heating, revealed two endothermic peaks: the invariant melting process of the ternary eutectic (212°C) and the liquidus temperature (226°C). For all the other samples, only one endothermic peak was detected on heating at an average temperature of 208°C; nevertheless, for the samples SAC_3, SAC_4 and SAC_5 a minimum value of 207°C was obtained. This effect corresponds to a melting temperature depression of about 10 °C in comparison with the melting temperature of the eutectic bulk alloy (see 3.2).

Zou et al. [51] studied by DSC at different scanning rate the melting and solidification properties of the Sn3.0Ag0.5Cu (mass%) NPs smaller than 100 nm, obtaining an average melting point depression of 7°C for a scanning rate of 6°/min. For nanoparticles with the average diameter of 18 nm, a melting point depression of 26.6 °C was measured by TG-DSC at a heating rate of 5°/min [44]. As an example, two heating cycle performed by DSC on the SAC_2 sample are shown in Fig. 7. In the first cycle (Fig.7a), after the endothermic peak assigned to the ternary invariant reaction, it is possible to recognize a small exothermic peak ascribed to the re-crystallization of the SnOx amorphous layer surrounding the particles (see 3.1). This small exothermic peak was not recorded in the second cycle thermogram (Fig.7b). The comparison of the XRD patterns before and after DSC confirms our results, and are in agreement with those reported by Koppes et al.[40] for Sn NPs.

The DSC cooling curves for the SAC samples (Fig. 8) are comparable to those obtained and discussed in *section 3.1* for the SnAg nanopowders (see, for instance, Fig. 4b), showing a series of fluctuating exothermic peaks between 190 and 90°C with a sharp peak around 150°C, that we assume corresponding to the solidification.

Similar trend in the cooling curves was reported for SAC alloys [42,51], although the small magnification of the graphs does not allow a comprehensive discussion. Zou et al. [51] by DSC measurements observed a large (>88°) undercooling for SAC NPs, which results from the energy barrier for solid nucleation, and the value reported is fairly in agreement with the present results (approximately 67°C).

On heating, an exothermic peak around 240°C (300°C, at the top of the peak) was recorded only for the samples SAC_5 and SAC_6 treated with citric acid, similarly to the prominent exothermic peak observed around 260°C by Roshanghias et al. [44]. We can assume that the addition of the

citric acid to the aqueous solution enhanced the thickness of the amorphous SnOx layer on the NPs surface, instead of removing it, as reported by Yung et al. [41]. Indeed, after DSC, the XRD patterns of citric acid treated samples, i.e. SAC_5 and SAC_6, show a higher intensity of the SnO peaks in comparison with XRD of untreated SAC samples.

A quantitative evaluation of the SAC NPs melting enthalpy indicates a value of 50±2 J/g, in comparison with the value of 67.0 J/g reported for the Sn3.0Ag0.5Cu (mass%) bulk alloy [52].

The morphological aspect of the SAC_2 sample after two DSC heating cycles is shown in Fig. 9. At lower magnification, the SE signal (Fig.9a) shows micrometric spherical particles dusted with SnO flakes. At higher magnification, the BSE signal (Fig. 9b) allows to reveal in the bigger particles the typical SnAgCu ternary eutectic consisting of Ag_3Sn plates and Cu_6Sn_5 rods in a (βSn) matrix, which is comparable with the morphology of the eutectic bulk SAC alloy (see Fig. 9c).

3.2.3. Melting temperature depression: Theory vs. experiment

The melting behaviour of eutectic SnAg and SAC nanoalloys has been investigated experimentally and theoretically. In both cases, the input data for calculations were taken from [3,53]. The experimental data for SnAg NPs obtained in the present work were compared with the melting curve predicted by the homogeneous melting model (HM model) [23] as well as the literature datasets [29,36,54-56], as shown in Fig. 10. A good agreement between analysed datasets and model predicted values can be observed.

Concerning SAC nanoalloys the new experimental data indicate the melting temperature depression values (Fig. 11) that lie between the corresponding HM (curve 1) and CALPHAD (curve 2) predicted values and exhibit a very good agreement with the data reported in [30,42,57]. The theoretical curve obtained by the CALPHAD method shows lower values compared to those calculated by the HM model (Fig. 11), as reported in [30]. Similar observations were found for SnAg [29] and AgCu NPs [31]. The melting temperature of investigated SnAg and SAC nanoalloys decreases drastically for particles with a size below 20 nm (Figs. 9 and 10).

4. Conclusions

SnAg and SnAgCu nanoparticles at the eutectic composition have been successfully synthesized by a low temperature chemical reduction method. The formation of the phases pertaining to the binary and ternary eutectics has been confirmed by XRD analysis.

The melting properties of the NPs were studied by a high sensitive DSC and a melting temperature depression of 7-10°C was observed for both systems. The melting enthalpies measured from the area under the DSC heating curves of the SnAg and SnAgCu NPs are very similar (49±2 and 50±2 J/g. respectively); these values are lower than those reported in literature for the corresponding bulk alloys.

After DSC analysis, micrometric spheres having eutectic aspect dusted with smaller tin oxide particles were obtained for all samples, likewise observed in our previous work for the Bi-Sn NPs. Considering that during the investigation of the Ag-Cu NPs [31] we did not observe this behaviour (the samples after heating inside the DSC turned into small ingots), we can conclude that the proneness of tin to oxidation inhibit the complete aggregation of the nanoparticles after the melting process. The peculiar aspect of the SnAg and SnAgCu DSC curves observed on cooling is related to this phenomenon. The formation of the SnO_x layer around NPs could be detrimental for the employment of SnAg and SAC NPs in the joining technology.

The new experimental data on the melting temperature depression of SnAg and SAC eutectic nanoalloys exhibit a very good agreement with the literature datasets and are comparable to the HM or/and CALPHAD predicted values.

References

1. P.T. Vianco, D.R. Frear, Issues in the replacement of Pb-bearing solders, JOM 45 (1993) 14-19.

2. K.-W. Moon, W.J. Boettinger, U.R. Kattner, F.S. Biancaniello, C.A. Handwerker, Experimental and thermodynamic assessment of Sn-Ag-Cu solder alloys, J. Electron. Mater. 29 (2000) 1122-1236.

3. M.-Abtew, G.-Selvaduray, Lead-free Solders in Microelectronics, Materials Science and Engineering: R: Reports 27 (2000) 65-141.

4. K. Suganuma, The development and commercialization of lead-free soldering, MRS Bulletin 26(11) (2001) 880-884.

5. K.J. Rönkä, F.J.J van Loo, J.K. Kivilahti, The local nominal composition-useful concept for microjoining and interconnection applications, Scripta Mater. 37 (1997) 1575-1581.

6. J. Wu, S-b Xue, J-W Wang, S. Liu, Y.-L. Han, L.-J. Wang, Recent progress of Sn–Ag–Cu lead-free solders bearing alloy elements and nanoparticles in electronic packaging, J. Mater Sci: Mater. Electron. 27 (2016) 12729-12763.

7. D. Giuranno, S. Delsante, G. Borzone, R. Novakovic, Effects of Sb addition on the properties of Sn-Ag-Cu/(Cu, Ni) solder systems, J. Alloys Compd. 689 (2016) 918-930.

8. The European Action COST 531 project, 2008. (http://w3.cost.eu/fileadmin/domain_files/MAT/Action_531/final_report/final_report-531.pdf

9. Z. Moser, W. Gąsior, K. Bukat, J. Pstruś, R. Kisiel, J. Sitek, K. Ishida, I. Ohnuma, Pb-free solders: part 1. Testing of Sn-Ag-Cu alloys with Bi additions, J. Phase Equilib. Diff. 27 (2006) 133-139.

10. L.R. Garcia, W.R. Osorio, L.C. Peixoto, A. Garcia, Wetting behavior and mechanical properties of Sn-Zn and Sn-Pb solder alloys, J. Electron. Mater. 38(11) (2009) 2405-2414.

11. S.H. Park, D.S. Seo, J.K. Lee, Electrical Properties of Silver Paste Prepared from Nanoparticles and Lead-Free Frit, J. Nanosci. Nanotechnol. 7(11) (2007)3917-3919.

12. C. J. Yang, M. G. Cho, H. M. Lee, Synthesis of the Combination Solder of 80Au-20Sn/42Sn-58Bi and Thermodynamic Interpretation of the Microstructural Evolution, Mater. Trans. 49(2) (2008) 376-381.

13. W. Luc, C. Collins, S. Wang, H. Xin, K. He, Y. Kang, F. Jiao, Ag−Sn Bimetallic Catalyst with a Core−Shell Structure for CO_2 Reduction, J. Am. Chem. Soc. 139 (2017) 1885-1893.

14. R. Ferrando, J. Jellinek, R.L. Johnston, Nanoalloys: From Theory to Applications of Alloy Clusters and Nanoparticles, Chem. Rev. 108 (2008) 845-910.

15. F. Calvo, Thermodynamics of nanoalloys, Phys. Chem. Chem. Phys. 17 (2015) 27922-27939.

16. G. Borzone and S. Delsante, in Handbook of High-Temperature Lead-Free Solders, Thermodynamic Properties, Vol. 2, WG1 Materials Properties, Ed. A. Watson, Brno, Czech Republic, COST office, Brussels, Belgium, 2012, 7-96, ISBN: 978-80-905363-2-6.

17. R. Novakovic and Yu. Plevachuk, in Handbook of High-Temperature Lead-Free Solders, Thermophysical Properties, Vol. 2, WG1 Materials Properties, Ed. A. Watson, Brno, Czech Republic, COST office, Brussels, Belgium, 2012, 97-141, ISBN: 978-80-905363-2-6.

18. T. Tanaka, S. Hara, Thermodynamic evaluation of binary phase diagrams of small particle systems, Z. Metallkd. 92(5) (2001) 467-472.

19. T. Tanaka, Prediction of Phase Diagrams in Nano-sized Binary Alloys, Materials Science Forum, 653 (2010) 55-75.

20. K.Sim, J. Lee, Phase stability of Ag–Sn alloy nanoparticles, J. Alloys Compd., 590 (2014) 140-146.

21. M. Wautelet, J. P. Dauchot, M. Hecq, Phase diagrams of small particles of binary systems-a theoretical approach, Nanotechnology, 11 (2000) 6-9.

22. P. Pawlow, On the dependence of the melting point with the surface energy of solid materials, Z. Phys. Chem. 65 (1909) 545-548.

23. P. Buffat, J.P. Borel, Size effect on the melting temperature of gold particles, Phys. Rev. A, 13(6) (1976) 2287-2298.

24. C.J. Coombes, The melting of small particles of lead and indium, J. Phys. F: Metal Phys. 2 (1972) 441-449.

25. G. Guisbiers, G. Abudukelimu, F. Clement, M. Wautelet, Effects of Shape on the Phase Stability of Nanoparticles, J. Comput. Theor. Nanosci. 4 (2007) 309-315.

26. A. Barybin, V. Shapovalov, Modification of Pawlow's thermodynamical model for the melting of small single-component particles, J. Appl. Phys. 109 (2011) 034303.

27. L. Pavan, F. Baletto, R. Novakovic, Multiscale approach for studying melting transitions in CuPt nanoparticles, Phys. Chem. Chem. Phys. 17 (2015) 28364-28371.

28. G. Kaptay, J. Janczak-Rusch, G. Pigozzi, L.P.H. Jeurgens, Theoretical Analysis of Melting Point Depression of Pure Metals in Different Initial Configurations, J. Mater. Eng. Perform. 23(5) (2014) 1600-1607.

29. J. Sopoušek, J. Vřešťál, A. Zemanova, J. Bursik, Phase Diagram Prediction And Particle Characterisation of Sn-Ag Nano Alloy For Low Melting Point Lead-Free Solders, J. Min. Metall. Sect. B-Metall., 48 (3)B (2012) 419-425.

30. A. Roshanghias, J. Vrestal, A. Yakymovych, K.W. Richter, H. Ipser, Sn–Ag–Cu nanosolders: Melting behavior and phase diagram prediction in the Sn-rich corner of the ternary system, CALPHAD, 49 (2015) 101-109.

31. S. Delsante, G. Borzone, R. Novakovic, D. Piazza, G. Pigozzi, J. Janczak-Rusch, M. Pilloni, G. Ennas, Synthesis and thermodynamics of Ag–Cu nanoparticles, Phys. Chem. Chem. Phys. 17 (2015) 28387-28393.

32. B. L. Cushing, V. L. Kolesnichenko, C. J. O'Connor, Recent Advances in the Liquid-Phase Syntheses of Inorganic Nanoparticles, Chem. Rev., 104 (2004) 3893-3946.

33. S. Pande, A. K. Sarkar, M. Basu, S. Jana, A. K. Sinha, S. Sarkar, M. Pradhan, S.Saha, A.Pal, T. Pal, Synthesis of Lead-Free Solder in the Nanometer Length Scale Obtained from Tin and Silver Compounds Using Silicone Oil, Langmuir, 24 (2008) 8991-8997.

34. B.M. Munoz-Flores, B. I. Kharisov, V. M. Jimenez-Perez, P. E. Martinez, S. T. Lopez, Recent advances in the synthesis and main applications of metallic nanoalloys, Ind. Eng. Chem. Res. 50 (2011) 7705-7721.

35. Y. Xiong Metallic Nanostructures, X. Lu (Eds.), Springer International Publishing Switzerland, 2015.

36. C. Zou, Y. Gao, B.Yang, Q. Zhai, Synthesis and DSC study on Sn3.5Ag alloy nanoparticles used for lower melting temperature solder, J. Mater Sci: Mater Electron. 21 (2010) 868-874.

37. L-Y Hsiao, J-G Duh, Revealing the Nucleation and Growth Mechanism of a Novel Solder Developed from Sn-3.5Ag-0.5Cu Nanoparticles by a Chemical Reduction Method, J. Electron. Mater. 35 (2006) 1755-1759.

38. F. Frongia, M. Pilloni, A. Scano, A. Ardu, C. Cannas, A. Musinu, G. Borzone, S. Delsante, R. Novakovic, G. Ennas, Synthesis and Melting Behaviour of Bi, Sn and Sn-Bi Nanostructured Alloy, J. Alloys Compd. 623 (2015) 7-14.

39. L. Alexander, H.P. Klug, Determination of Crystallite Size with the X-Ray Spectrometer, J. Appl. Phys. 21 (1950) 137-142.

40. J.P. Koppes, K. A. Grossklaus, A.R. Muza, R.R. Revur, S. Sengupta, A. Rae, E.A. Stach, C. A. Handwerker, Utilizing the thermodynamic nanoparticle size effects for low temperature Pb-free solder, Materials Science and Engineering B, 177 (2012) 197-204.

41. K.C.Yung, C.M.T.Law, C.P.Lee, B.Cheung, T.M.Yue, Size control and characterization of Sn-Ag-Cu lead-free nanosolders by a chemical reduction process, J. Electr.Mater., 41(2) (2012) 313-321.

42. H. Jiang, K-s. Moon, C.P. Wong, Recent advances of nanolead-free solder material for low processing temperature interconnect applications, Microelectronics Reliability, 53 (2013) 1968-1978.

43. T.B. Massalski, H. Okamoto, P.R. Subramanian, L. Kacprzak (Eds.), Binary Alloy Phase Diagrams, 2nd edn. Vols. 1-3, ASM, International Materials Park, OH, 1990.

44. A. Roshanghias, A. Yakymovych, J. Bernardi, H. Ipser, Synthesis and thermal behavior of tin-based alloy (Sn–Ag–Cu) nanoparticles, Nanoscale, 7 (2015) 5843-5851.

45. M. Huh, S. Kim, J. Ahn, B. Kim, J. Park, Oxidation of nanophase tin particles, Nanostruct. Mater. 11 (1999) 211-220.

46. P. Song, D. Wen, Experimental Investigation of the Oxidation of Tin Nanoparticles, J. Phys. Chem. C, 113 (2009) 13470-13476.

47. I. Kaban, K. Khalouk, M. Ko¨ Hler, W. Hoyer, J.-G. Gasser, Physical Properties of Sn96.5Ag3.5-Based Solders with Additions of Bi, Ge, and In, J. Electr. Mater., 39(1) (2010) 70-76.

48. I. Ohnuma, M. Miyashita, K. Anzai, X.J. Liu, H. Ohtani, R. Kainuma, K. Ishida, Phase equilibria and the related properties of Sn-Ag-Cu based Pb-free solder alloys, J. Electron. Mater. 29(10) (2000) 1137-1144.

49. M.E. Loomans, M. E. Fine, Tin-Silver-Copper eutectic temperature and composition, Metall. Mater. Trans. A, 31A (2000) 1155-1162.

50. D. Lewis, S. Allen, M. Notis, A. Scotch, Determination of the eutectic structure in the Ag-Cu-Sn system, J. Electron. Mater. 31(2) (2002) 161-167.

51. C. Zou, Y. Gao, B. Yang, Q. Zhai, Melting and solidification properties of the nanoparticles of Sn3.0Ag.05Cu lead-free solder alloy, Mater. Charact. 61 (2010) 474-480.

52. Y. Gao, C. Zou, B. Yang, Q. Zhaia, J. Liu, E. Zhuravlev, C. Schick, Nanoparticles of SnAgCu lead-free solder alloy with an equivalent melting temperature of SnPb solder alloy, J. Alloys Compd. 484 (2009) 777-781.

53. T. Iida, R.I.L. Guthrie, The physical properties of liquid metals, 1st edn. Clarendon Press, Oxford, 1993.

54. H. Jiang, K.S. Moon, F. Hua, C.P. Wong, Synthesis and Thermal and Wetting Properties of Tin/Silver Alloy Nanoparticles for Low Melting Point Lead-Free Solders, Chem. Mater. 19(18) (2007) 4482-4485.

55. T.T. Bao, Y. Kim, J. Lee, J.-G. Lee, Preparation and Thermal Analysis of Sn-Ag Nano Solders, Mater. Trans. 51(12) (2010) 2145-2149.

56. R.N. Chukka, S. Telu, B. NRMR, L. Chen, A novel method of reducing melting temperatures in SnAg and SnCu solder alloys, J. Mater. Sci.: Mater. Electron. 22(3) (2011) 281-285.

57. C. Zou,Y. Gao, B. Yang, Q. Zhai, Nanoparticles of Sn3.0Ag0.5Cu alloy synthesized at room temperature with large melting temperature depression, J. Mater. Sci.: Mater. Electron. 23(1) (2012) 2-7.

Figures Captions

Fig. 1 XRD patterns of the SA_8 sample "as-prepared" and after DSC analysis.

Fig. 2 XRD pattern of the SA_11 sample "as-prepared" and after DSC analysis.

Fig.3 DSC heating (a) and cooling (b) curves of the SA_8 sample.

Fig. 4 DSC heating (a) and cooling (b) curves of the SA_11 sample.

Fig. 5 Secondary electron (SE) (a) and Backscattered electron (BSE) (b) images of the SA_8 sample after DSC measurements.

Fig. 6 XRD pattern of the SAC_2 sample "as-prepared" and after DSC analysis.

Fig. 7 Sample SAC_2. DSC curves: first heating cycle (a) and second heating cycle (b).

Fig. 8 Sample SAC_2. DSC curves: first cooling cycle (a) and second cooling cycle (b).

Fig.9 SE (a) and BSE (b) images of the SAC_2 sample after DSC measurements. BSE (c) image of eutectic bulk SAC alloy: light gray βSn phase, together with Ag_3Sn elongated plates, and Cu_6Sn_5 blocky particles.

Fig. 10 The melting temperature dependence of the SnAg eutectic nanoalloy as a function of particle size calculated by the HM model [23] together with the experimental data shown for a comparison: (✶) present work, (●) [29], (■) [54], (▼) [36], (+) [55], (▲) [56]. (------) the melting temperature of the eutectic bulk alloy.

Fig. 11 The melting temperature dependence of the SAC eutectic nanoalloy as a function of particle size calculated by the HM model [23] (curve 1) together with the experimental data shown for a comparison: (✶) present work, (○) [30], (●) [44], (■) [57], (▲) [42], (▼) [52]. CALPHAD predicted values [30] (curve 2); (------) the melting temperature of the eutectic bulk alloy.

Graphical Abstract (for review)

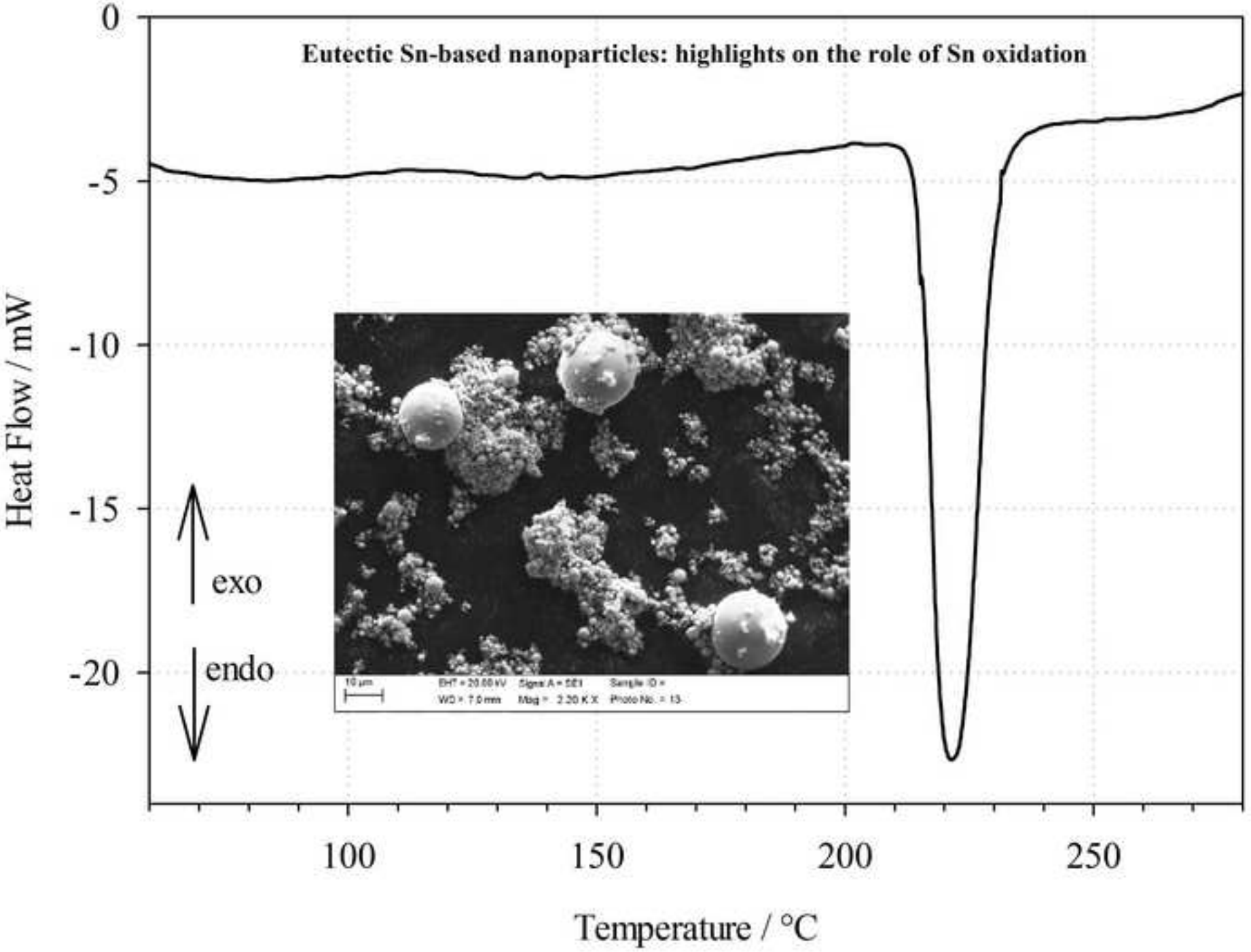

Highlights

- SnAg and SnAgCu nanoparticles at the eutectic composition have been synthesized
- A melting temperature depression of 7-10°C was determined for both systems by DSC
- Melting enthalpy values of the NPs are lower than the corresponding bulk alloys
- The role of tin oxidation on the aggregation of eutectic Sn-based NPs is presented
- Experimental results are compared to the predicted values and available datasets

Table

Table 1: SnAg (SA_#) and SAC (SAC_#) nanopowders synthesised in anhydrous methanol + 1,10 phenanthroline (if not differently specified).

Sample	XRD analyses detected phases		Melting temperature /°C	Remarks
	As prepared	After DSC		
SA_1	Ag_3Sn + βSn		214	
SA_2	Ag_3Sn + βSn		214	
SA_3	Ag_3Sn + βSn	Ag_3Sn + βSn + SnO +(SnO_2)	212	
SA_4	Ag_3Sn + βSn	Ag_3Sn + βSn + SnO	214	
SA_5	Ag_3Sn + βSn	Ag_3Sn + βSn + SnO	214	
SA_6	Ag_3Sn + βSn	Ag_3Sn + βSn + SnO	216	
SA_7 (a)	Ag_3Sn + βSn	Ag_3Sn + βSn + SnO	214	
SA_8	Ag_3Sn + βSn	Ag_3Sn + βSn + SnO	214	Fig. 1 (XRD) Fig. 3a e 3b (DSC) Fig.5 (SEM)
SA_9	Ag_3Sn + βSn	Ag_3Sn + βSn + SnO	215	
SA_10 (a)	Ag_3Sn + βSn	Ag_3Sn + βSn + SnO + (SnO_2)	211	
SA_11 (b)	Ag_3Sn + βSn	Ag_3Sn + βSn + SnO	211	Fig. 2 (XRD) Fig. 4a e 4b (DSC)
SAC_1 (b)	Ag_3Sn + βSn + Cu_6Sn_5		212 (liquidus at 226)	Off-stoichiometry (see text)
SAC_2 (b)	Ag_3Sn + βSn + Cu_6Sn_5	Ag_3Sn + βSn + Cu_6Sn_5 + SnO	210, 1st heating cycle 213, 2nd heating cycle	Fig. 6 (XRD) Figs. 7 and 8 (DSC) Fig. 9 (FE-SEM)
SAC_3 (b)	Ag_3Sn + βSn + Cu_6Sn_5	Ag_3Sn + βSn + Cu_6Sn_5 + SnO +(SnO_2)	207	Synthesis performed in MilliQ-water
SAC_4 (b)	Ag_3Sn + βSn + Cu_6Sn_5	Ag_3Sn + βSn + Cu_6Sn_5+ SnO + (SnO_2)	207	Synthesis performed in MilliQ-water
SAC_5	Ag_3Sn + βSn + Cu_6Sn_5	Ag_3Sn + βSn + Cu_6Sn_5 + SnO + (SnO_2)	207	NPs SAC_4 treated with Citric Acid for 1h.
SAC_6	Ag_3Sn + βSn + Cu_6Sn_5	Ag_3Sn + βSn + Cu_6Sn_5+ SnO + (SnO_2)	209	NPs SAC_4 treated with Citric Acid for 18h,

(a) Synthesis without 1,10 phenanthroline, (b) Tin precursor $SnCl_2$

Figure

Click here to download high resolution image

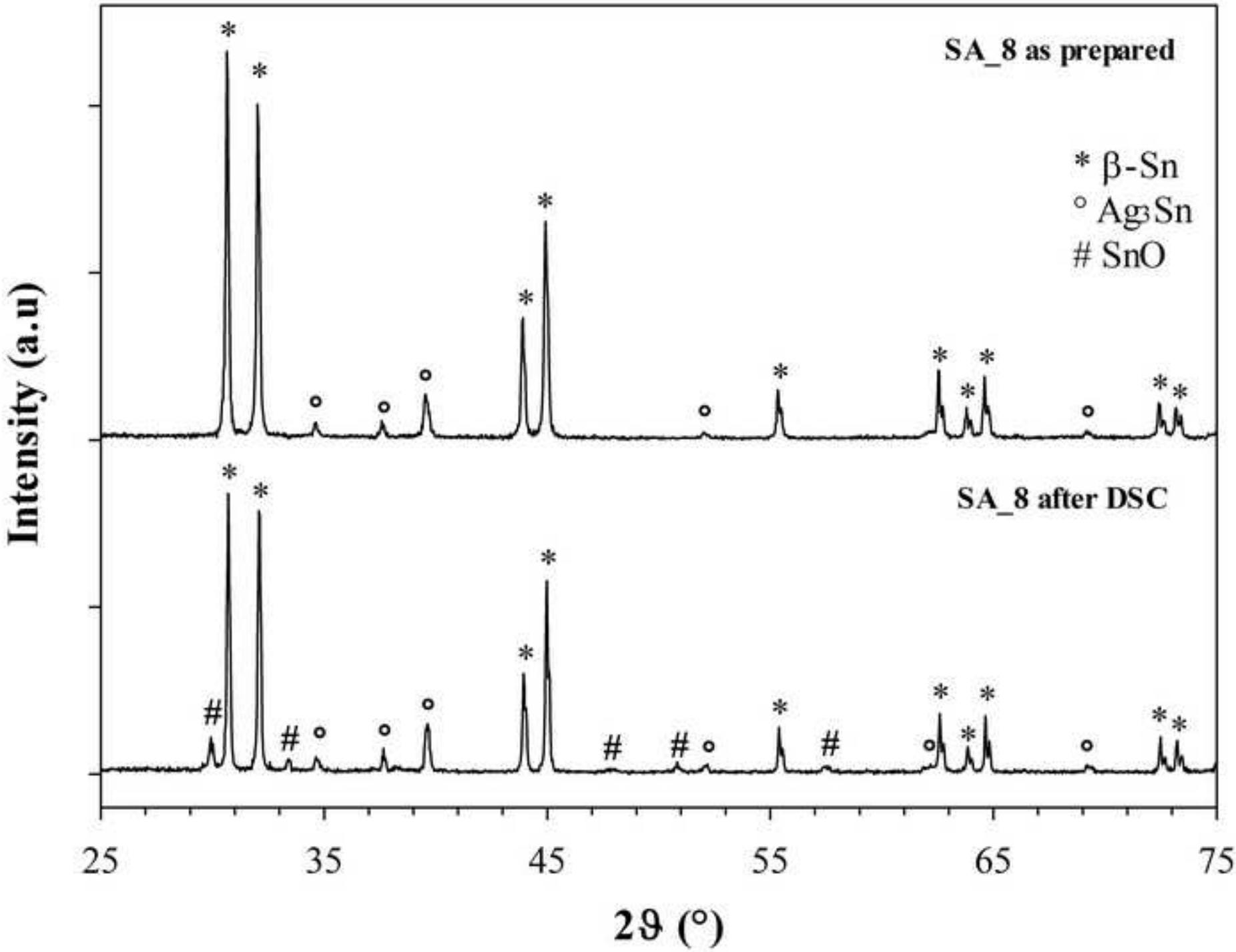

Figure

Click here to download high resolution image

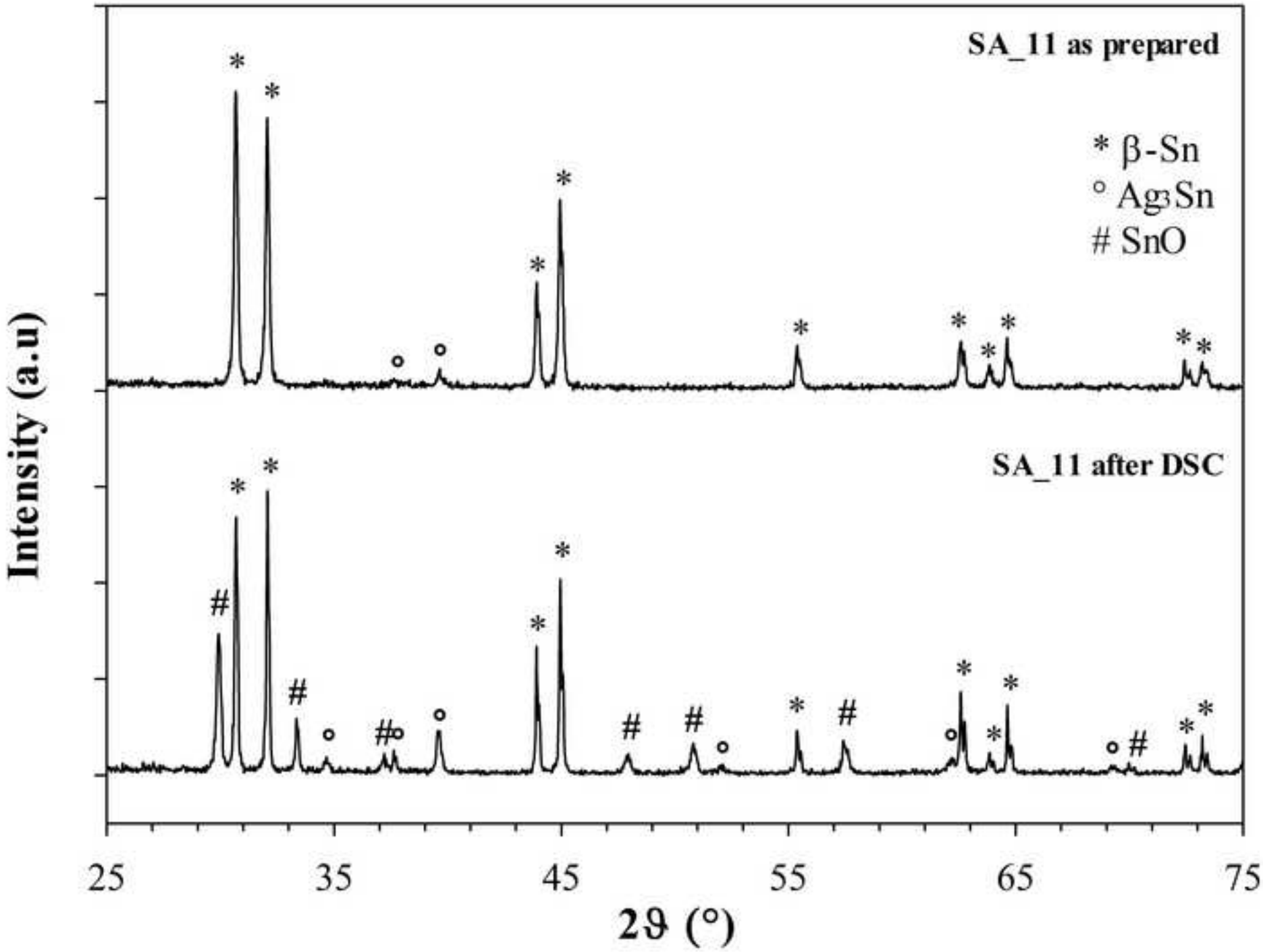

Figure
Click here to download high resolution image

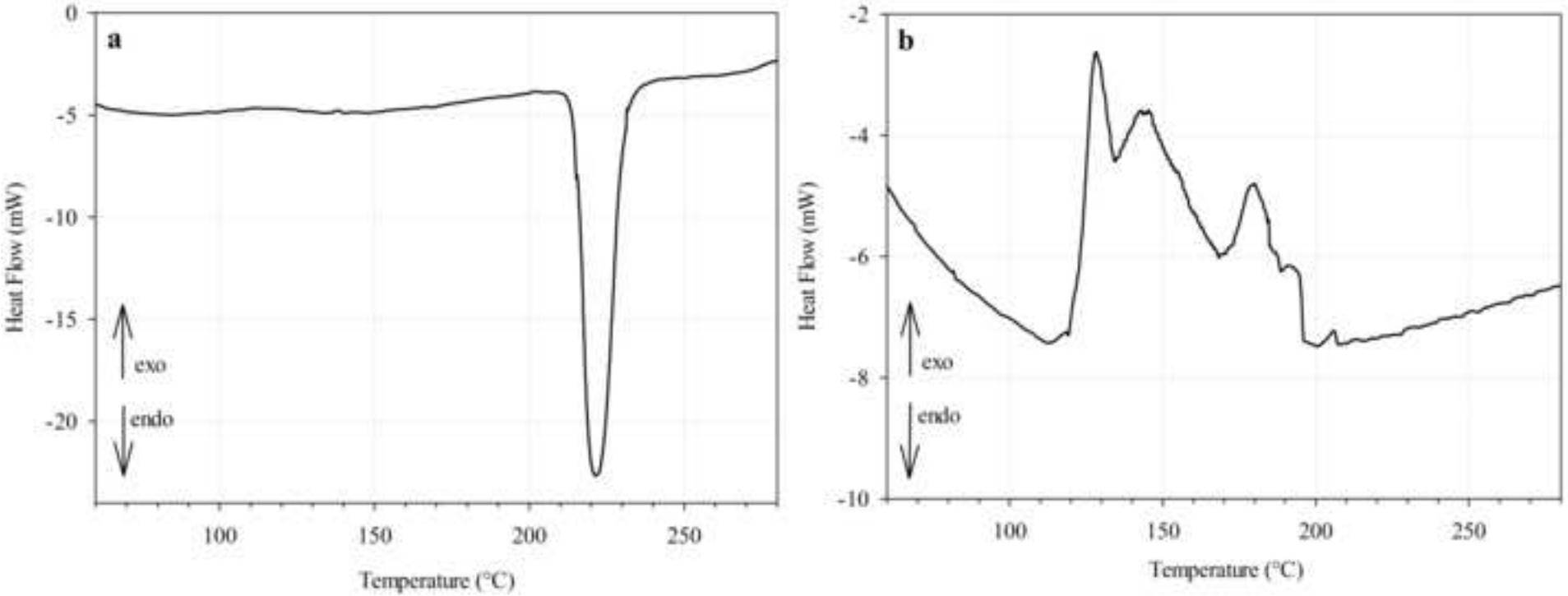

Figure
Click here to download high resolution image

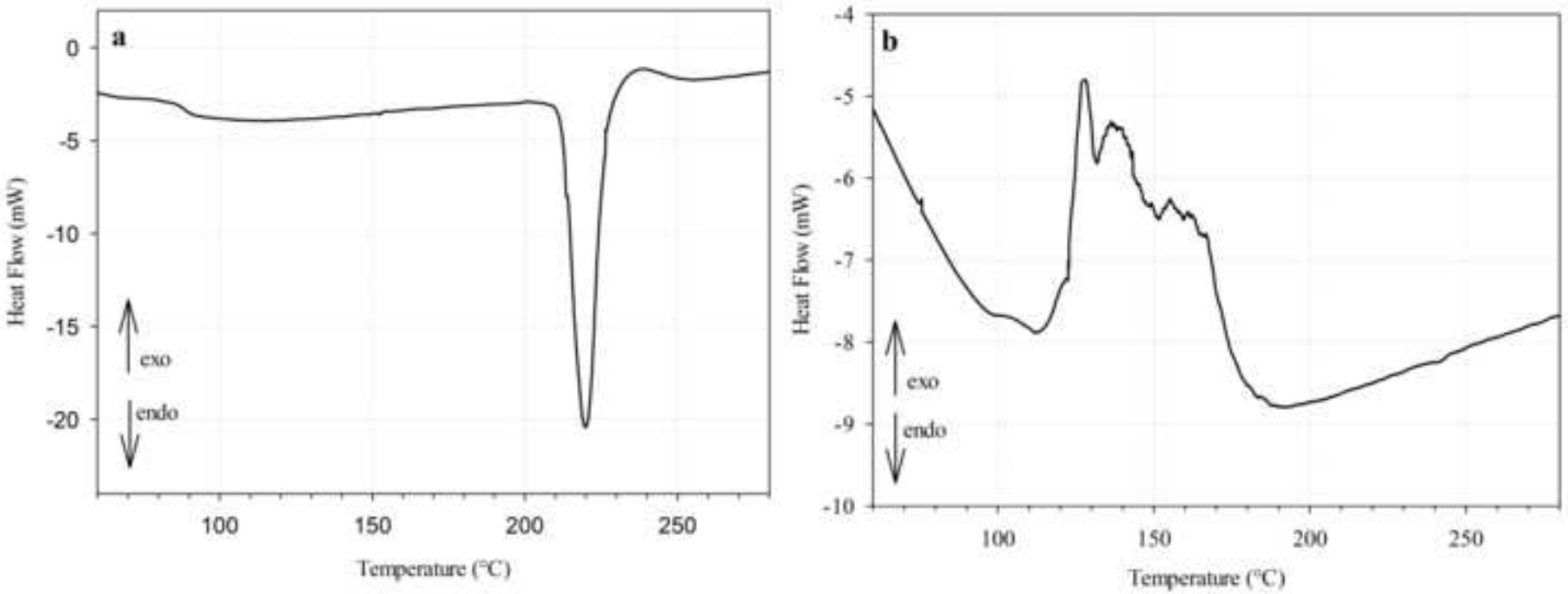

Figure

Click here to download high resolution image

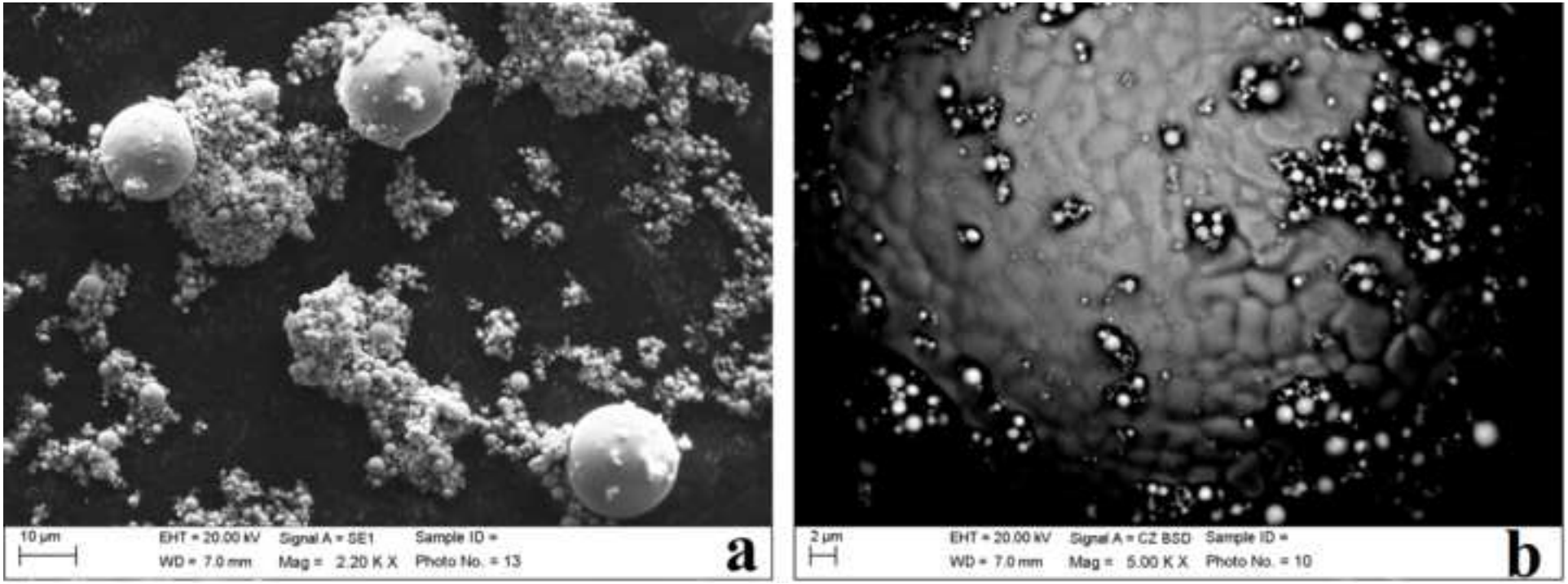

Figure
Click here to download high resolution image

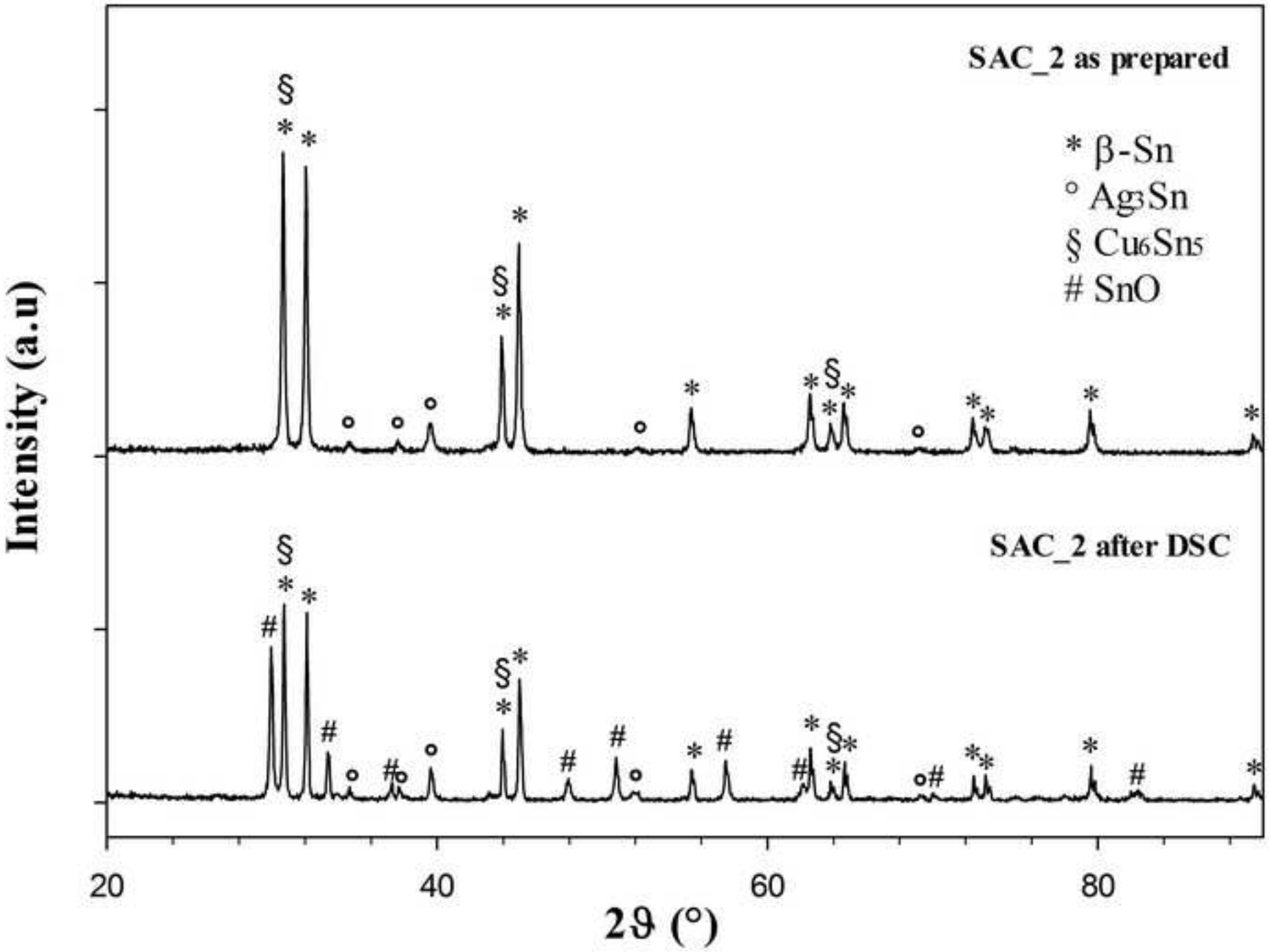

Figure

Click here to download high resolution image

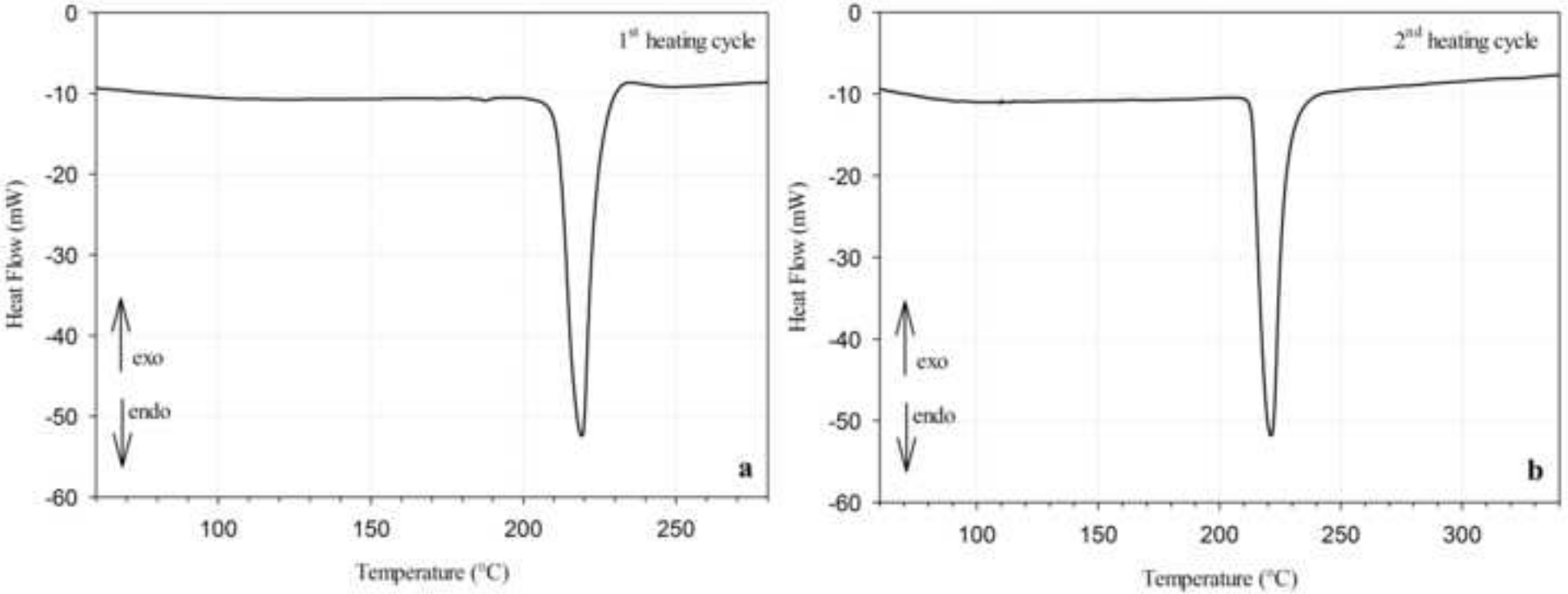

Figure
Click here to download high resolution image

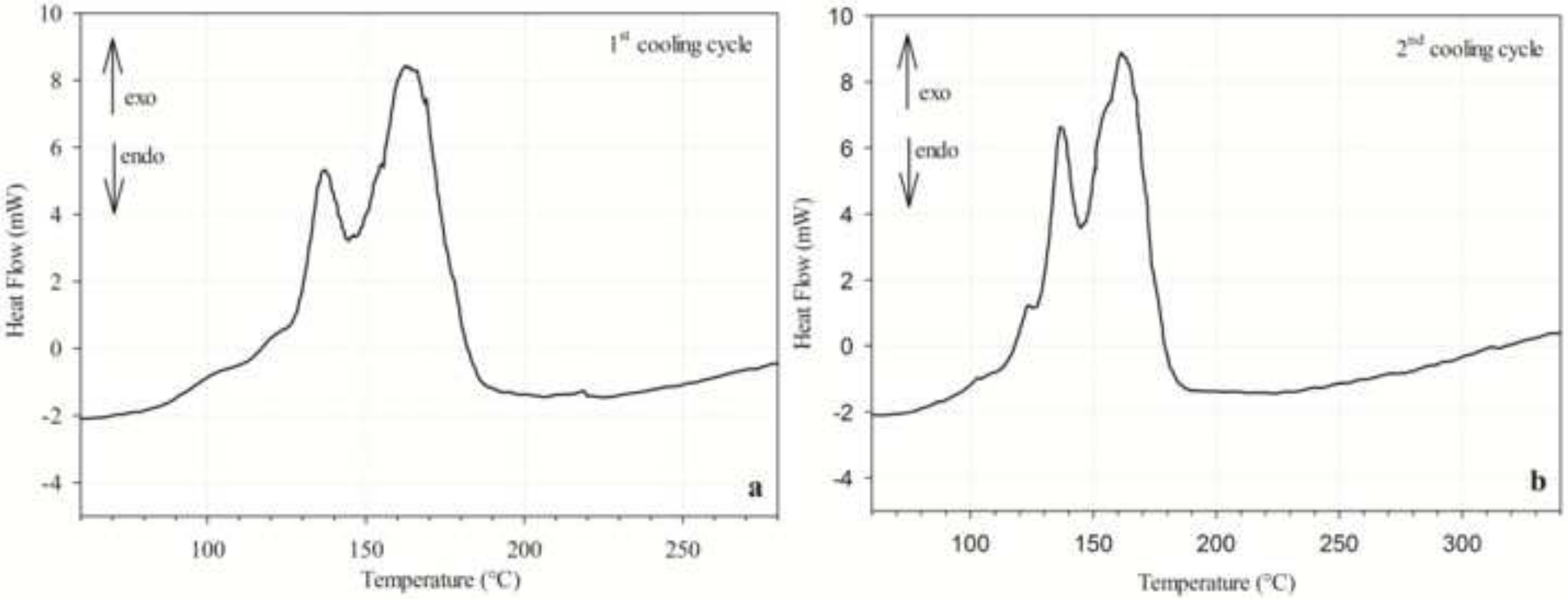

Figure

Click here to download high resolution image

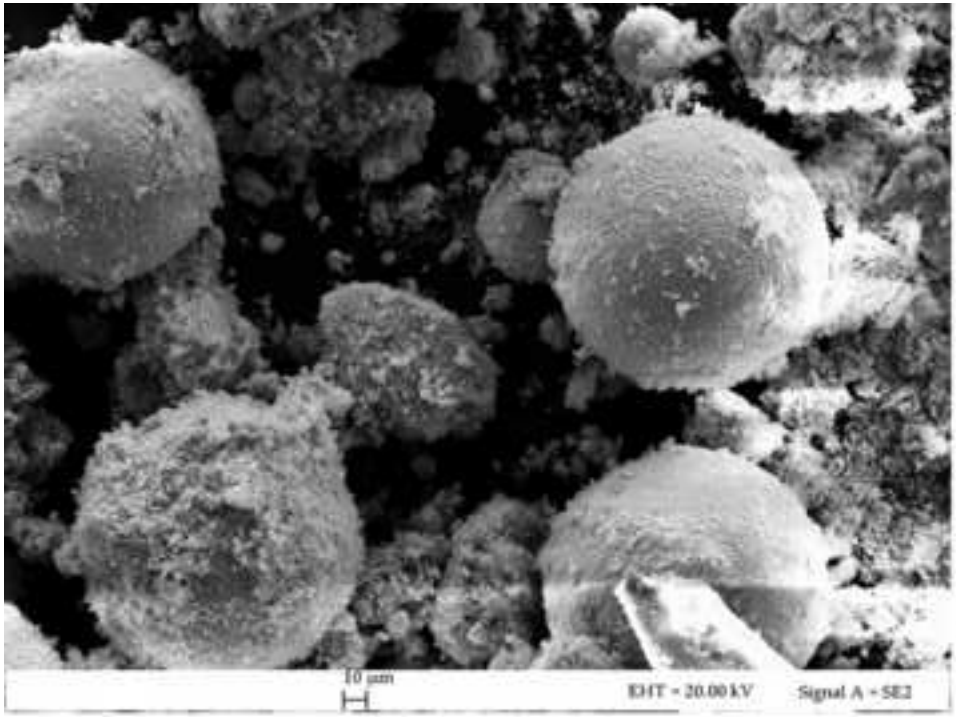

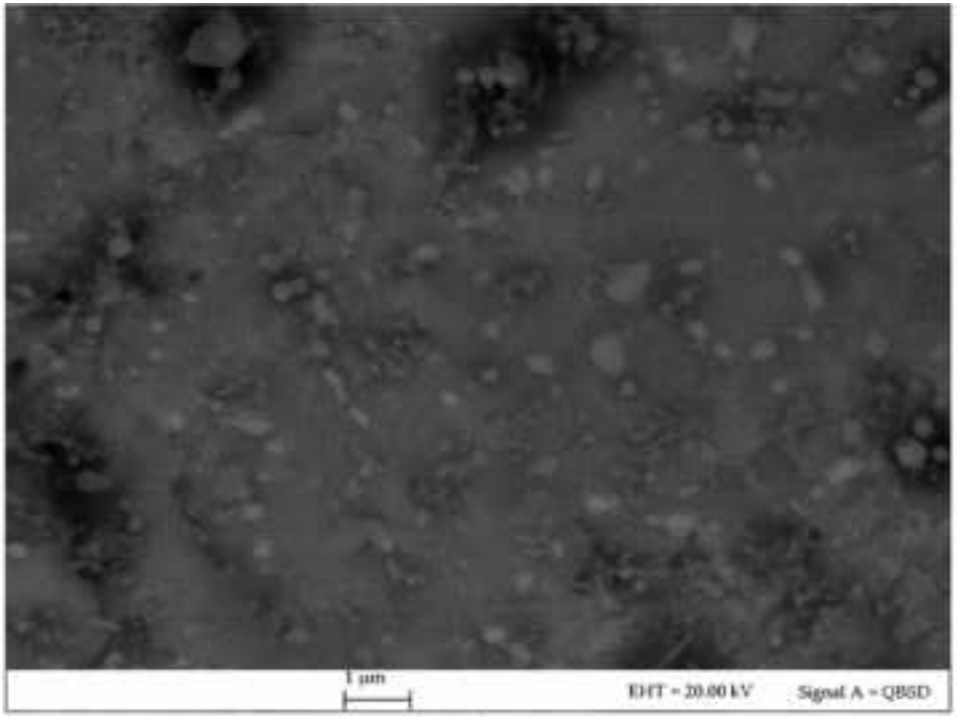

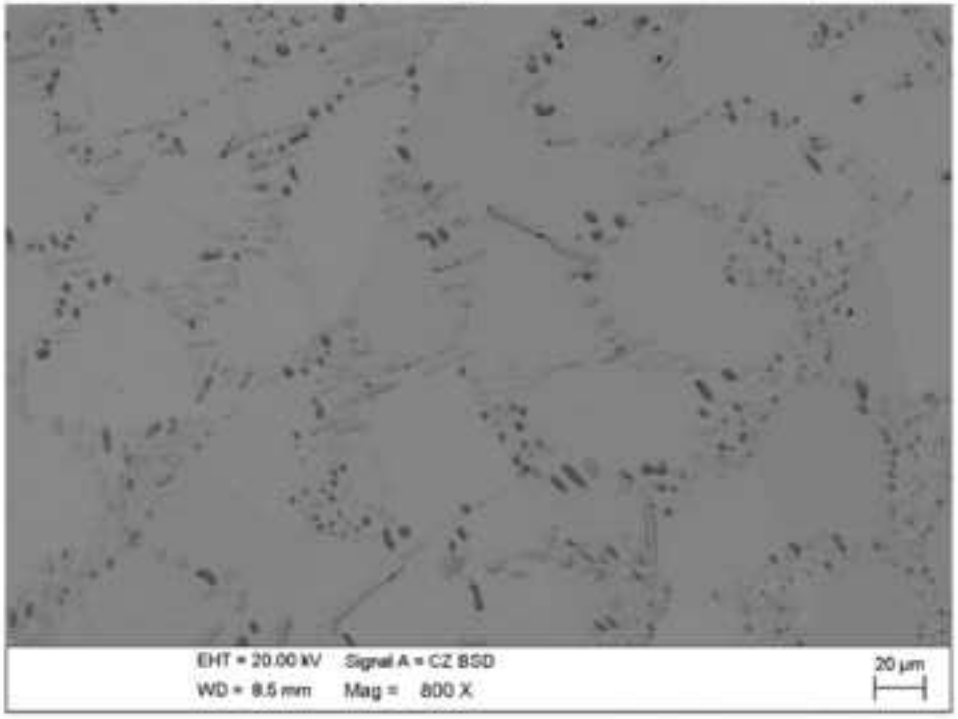

Figure

Click here to download high resolution image

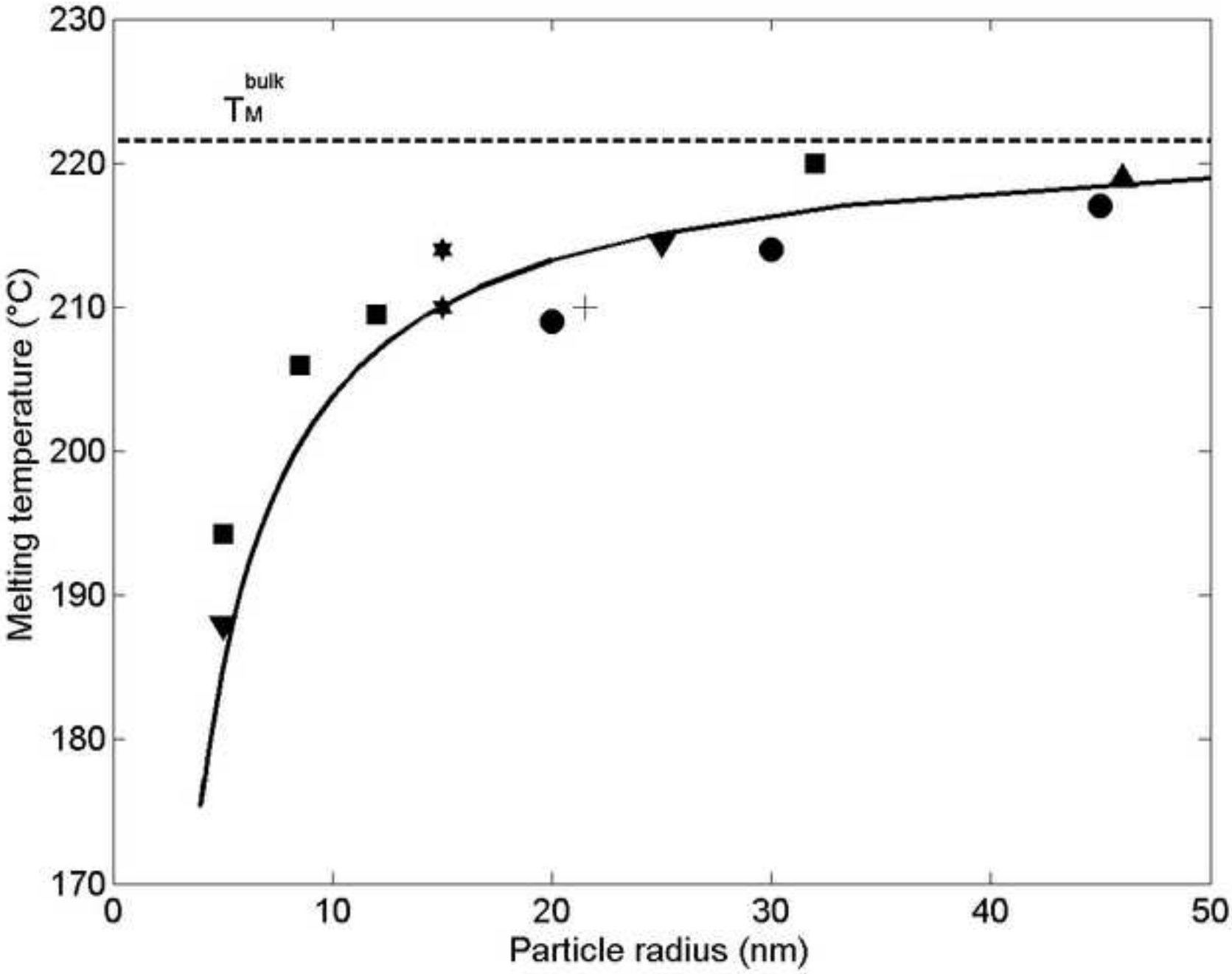

Figure
Click here to download high resolution image